

pubs.acs.org/est Article

# Using Street View Imagery to Predict Street-Level Particulate Air Pollution

Meng Qi and Steve Hankey\*



Cite This: Environ. Sci. Technol. 2021, 55, 2695-2704



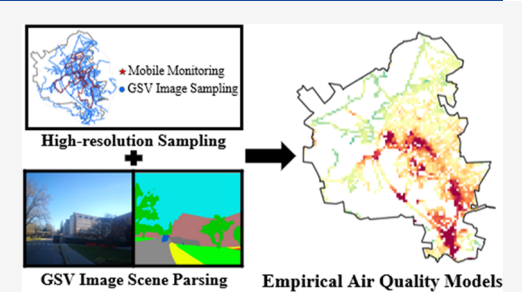
**ACCESS** 

Metrics & More



Supporting Information

ABSTRACT: Land-use regression (LUR) models are frequently applied to estimate spatial patterns of air pollution. Traditional LUR often relies on fixed-site measurements and GIS-derived variables with limited spatial resolution. We present an approach that leverages Google Street View (GSV) imagery to predict street-level particulate air pollution (i.e., black carbon [BC] and particle number [PN] concentrations). We developed empirical models based on mobile monitoring data and features extracted from ~52 500 GSV images using a deep learning model. We tested theory- and data-driven feature selection methods as well as models using images within varying buffer sizes (50–2000 m). Compared to LUR models with traditional variables, our models achieved similar model



performance using the street-level predictors while also identifying additional potential hotspots. Adjusted  $R^2$  (10-fold CV  $R^2$ ) with integrated feature selection was 0.57–0.64 (0.50–0.57) and 0.65–0.73 (0.61–0.66) for BC and PN models, respectively. Models using only features near the measurement locations (i.e., GSV images within 250 m) explained ~50% of air pollution variability, indicating PN and BC are strongly affected by the street-level built environment. Our results suggest that GSV imagery, processed with computer vision techniques, is a promising data source to develop LUR models with high spatial resolution and consistent predictor variables across administrative boundaries.

#### 1. INTRODUCTION

The negative impacts of air pollution exposure on human health have been shown by many epidemiological studies. 1-4 Since air pollutant concentrations can vary rapidly over short distances, 5,6 accurately estimating the spatial patterns of air pollution is important for assessing human exposure and health outcomes.<sup>7,8</sup> Numerous studies use measurements from fixed-site monitoring networks.<sup>9–12</sup> However, stationary monitoring is often cost-prohibitive, and thus sparsely distributed, which may lead to undetected hotspots and poor characterization of air quality at small spatial scales. 13-16 Compared to fixed-site monitoring, mobile monitoring offers an alternate approach to capture the spatial variation of street-level air pollution. 5,6 For example, Apte et al.<sup>5</sup> used Google Street View (GSV) cars to map air pollution at a spatial precision 4-5 orders of magnitude greater than that of routine monitoring stations. Consequently, empirical models based on dense mobile measurements may have the potential to better characterize street-level variation of air pollution to better describe health disparities at small spatial scales.

Land-use regression (LUR) is one type of empirical model which has been frequently applied to predict ambient air pollutant concentrations. Typically, LUR models use measurements from fixed-site monitoring networks and predictor variables derived from Geographic Information Systems (GIS) including land-use types, traffic intensity, and population density. While emerging studies use mobile monitoring data to increase the spatial density of measure-

ments used in LUR models, 22-25 other limitations arise when using traditional GIS-derived predictor variables that do not match the resolution of the mobile monitoring data. For example, GIS-derived variables are often jurisdiction specific since those data are usually collected to serve local administrative purposes. 26,27 Similarly, variables available at larger geographic scales (e.g., national) often provide less specific and spatially precise information. Since there are many mobile monitoring efforts being conducted across the world (which offer significant improvements in the spatial density of measurements), additional work is needed to develop predictor variables that (1) match the spatial scale of the measurements being collected and (2) are able to be derived in a consistent way across administrative and political boundaries. To address these limitations, we propose an image-derived empirical modeling approach that utilizes GSV imagery to extract streetlevel features as predictor variables.

Since its launch in 2007, GSV has collected a massive quantity of panoramic images across the world providing views of streetscapes at the eye level.<sup>28</sup> GSV imagery is becoming a

Received: August 18, 2020 Revised: December 11, 2020 Accepted: January 25, 2021 Published: February 4, 2021





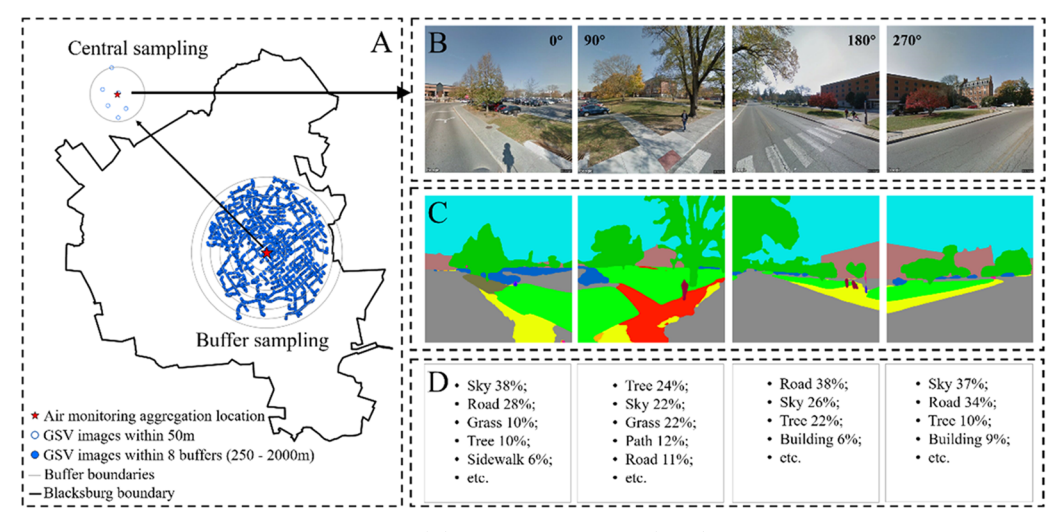


Figure 1. Image sampling and feature extraction procedure. (A) Google Street View (GSV) images sampled around one air pollutant monitoring aggregation location. (B) GSV images retrieved for four directions at one GSV sampling location. (C) Feature extraction using PSPNet scene parsing. (D) Estimated feature percentage among the 150 segmented classes.

reliable data source<sup>26,28,29</sup> and a promising tool for research studies owing to high spatial resolution, extensive coverage, open access to the public, and data consistency—especially when combined with computer vision techniques.<sup>30–32</sup> Previous studies have used GSV images in various ways, for example, estimating the demographic makeup of neighborhoods,<sup>30</sup> assessing urban vegetation and green space,<sup>33–35</sup> auditing neighborhood built environments,<sup>26,36</sup> automating land-use classifications,<sup>37</sup> or capturing changes in physical urban environments.<sup>38</sup> An emerging research area is using GSV imagery in air pollution research<sup>39</sup> to map hyperlocal air quality or to identify emission sources.

In this study, we investigate the use of GSV imagery to predict street-level particulate air pollution. In previous work, 24 we used a bicycle mobile monitoring platform to measure black carbon (BC) and particle number (PN) concentrations and developed LUR models based on traditional predictor variables. Based on the same air pollution measurements, we present here a series of empirical models with a promising new set of predictor variables: features extracted from GSV imagery by a deep learning scene parsing technique.<sup>32</sup> The models are built solely with features from GSV images. Three different feature selection methods (i.e., theory-driven, data-driven, and integrated) are tested during model development to improve model robustness and interpretability. Our results demonstrate that the combination of mobile monitoring and street scene images, assisted by computer vision techniques, constitutes a promising modeling approach to estimate air pollution at the street level.

# 2. MATERIALS AND METHODS

**2.1. Mobile Monitoring Data.** Mobile monitoring data was collected in a previous study, and full details of the monitoring campaign are described in Hankey et al. <sup>24</sup> Briefly, we conducted a bicycle mobile monitoring campaign to sample daytime street-level particulate air pollution in a small rural town (Blacksburg, VA) in 2016. We deployed microaethalometers (AE51; AethLabs) on bicycles to measure BC concentrations and condensation particle counters (CPC 3007; TSI, Inc.) to measure PN concentrations. Two mobile monitoring routes, each ~20 km in length, were repeatedly

sampled and ~120 h of mobile monitoring data was collected. We applied spatial aggregation at 100 m intervals along the routes, and the median concentrations of observations were tabulated for each aggregation location (n = 422 aggregation locations). We tested different methods to adjust mobile monitoring data for background concentrations in Hankey et al. 24 In this study, we used concentrations adjusted by the multiplicative method, which aims to best approximate longterm air pollution concentrations, for model development. Briefly, the multiplicative background adjustment method calculated adjustment factors based on the ratio of the daily concentration to the hourly concentration at a central site used to measure background concentrations. Then, the adjustment factors were applied to all mobile monitoring observations (based on the hour the mobile measurements were collected) to correct for variations in background concentrations.

2.2. Street-Level Predictor Variables. Unlike traditional LUR models, the predictor variables in this study were features extracted from GSV imagery, which capture street-level characteristics of the built and natural environment. GSV images were sampled around each mobile monitoring aggregation location including (1) central sampling, which randomly retrieved six locations of GSV imagery within 50 m of the aggregation locations and (2) buffer sampling where we created a 100 m × 100 m grid within 2000 m of each aggregation location and then repeated the central sampling approach for the centroid of each grid cell (Figure 1). GSV images within the 2000 m buffer were further stratified into eight circular buffers with radii ranging from 250 to 2000 m. Since GSV images are 360° photos, we retrieved four flat GSV images (640 × 640 pixels) at 90° intervals for each GSV sampling point. This procedure resulted in up to 24 images around each monitoring location or grid cell centroid depending on the availability of GSV images. To best match the mobile monitoring campaign, we preferentially collected GSV images photographed during the same year (2016). Images from the next closest year were included when year 2016 images were not available.

We used the Pyramid Scene Parsing Network (PSPNet), a deep learning model with state-of-the-art performance on various data sets, to process GSV images.<sup>32</sup> Feature extraction

was implemented at the pixel-wise level, i.e., each pixel in an image was classified into a specific feature. A total of 150 features were segmented, including natural features (e.g., trees, grass, plants), built environment features (e.g., roads, buildings, houses), and transportation features (e.g., cars, buses, vans). The percentage of each feature within an image was calculated (Figure 1D). The mean percentage of features among all images within a given buffer, representing the overall characteristics of that area, were used as street-level predictor variables for our empirical air quality models.

**2.3. Modeling Approach.** We developed GSV-only empirical models with predictor variables solely extracted from GSV images. To make direct comparisons with models using traditional variables, we used the same air pollution measurements and employed the same step-wise linear regression approach used by Hankey et al. <sup>24</sup> Briefly, the model uses a forward selection procedure, adding the variable which has the highest correlation with the dependent variable and subsequently adding the variable which is most correlated with model residuals. The process was repeated until the added variable was either not statistically significant (p < 0.05) or the model had unacceptably high multicollinearity (Variance Inflation Factor VIF > 5). All BC and PN concentrations were log transformed during model development and were transformed back to original values for model prediction.

To fully explore the role of GSV imagery in estimating street-level air pollution, we developed two types of GSV-only models: buffer-feature models and central-feature models. Buffer-feature models included both central features (i.e., the mean percentage of features for images within 50 m of aggregation locations) and buffer features at various spatial scales (i.e., eight circular buffers from 250 to 2000 m). During model development, each feature class was restricted to only be selected at a single buffer size. We also built central-feature models that only used features within 50 m of measurement locations to assess the ability of using only images very near measurement sites to explain air pollution variability. A sensitivity analysis was developed to investigate how the choice of spatial scale of the central features (i.e., by varying the radius size that defines central features) impacts model performance. Specifically, we collected features from GSV images within 250, 500, 750, and 1000 m of the mobile monitoring routes. Then, we compared central-feature models for each fixed radius.

Adjusted  $R^2$  and root-mean-square error (RMSE) were used as metrics to compare model performance. To evaluate model robustness and generalizability, 10-fold cross validation was conducted for each model. Specifically, the data was randomly partitioned into 10 subsets. Then we held out each subset and used the remaining nine subsets to build a model and predict the data for the hold out subset.  $R^2$  was calculated after all subsets were predicted. We repeated the 10-fold cross validation 10 times. The mean  $R^2$  was reported as the final 10-fold cross-validation  $R^2$ .

**2.4. Feature Selection.** We used a previously developed algorithm (PSPNet) to classify pixels in GSV images. <sup>32</sup> Upon inspection of all 150 classes extracted from the images, we found that many classes are irrelevant to air pollution; furthermore, as expected, some pixels were misclassified during scene parsing. Including irrelevant and spurious features in empirical air quality models may cause overfitting and reduce accuracy when applying the models. It also makes it difficult to interpret the selected variables and their coefficients. One way

to mitigate these problems is to conduct feature selection during the modeling process. 40,41 In this study, we tested three feature selection methods to develop GSV-derived predictor data sets to offer to our empirical air quality models. To avoid confusion, we refer to feature selection in this paper as the procedure used to assemble a subset of the 150 features extracted from the GSV imagery to offer to our empirical air quality models; this process is independent of the variable selection process used within the step-wise regression. The three feature selection methods include: (1) theory-driven feature selection, (2) data-driven feature selection, and (3) integrated feature selection, which is the combination of the first two approaches. In general, theory-driven feature selection utilizes subjective background knowledge accumulated among many studies, while data-driven feature selection solely relies on statistical characteristics of the data itself.

We designed our theory-driven feature selection based on our prior knowledge of air pollution. To illustrate this approach, we developed three categories of predictor variables derived from GSV images to offer to our air quality models: (1) "All variables" which included all 150 features, (2) "Theory-driven: Outdoor variables" which only included features that are commonly outdoors (n = 57), and (3) "Theory-driven: Air pollution-related variables" which only included features that may influence air pollution concentrations (n = 31). A full list of variables in each category as well as the reason for each variable being included or excluded from each category is listed in Table S1.

As a contrast to theory-driven feature selection, we designed our data-driven feature selection simply based on quantitative data filters without using any prior knowledge of air pollution. We used two data-filtering criteria and applied them to the "All variables" category. First, we filtered predictor variables based on the variable mean value averaged among all model building locations. The thresholds (i.e.,  $1\times 10^{-6}$ ,  $1\times 10^{-5}$ , and  $1\times 10^{-4}$ ) were determined by the statistical distribution shown in Figure S1. Second, we filtered predictor variables based on the nonzero percent of features among the aggregation locations. The thresholds were set to be equally distributed: 0, 20, 40, 60, and 80%. A total of 15 scenarios were then created based on the combination of these criteria. Both criteria aim to remove uncommon features in the study area from the model building data set. More details are described in the SI.

Integrated theory- and data-driven feature selection was applied to leverage the strengths of both approaches. These models used the same data-filtering criteria by the data-driven approach and applied them to the categories of predictor variables created by the theory-driven approach. To simplify model comparison, the best models among scenarios within the data-driven or integrated feature selection approaches were chosen based on the highest 10-fold CV  $\mathbb{R}^2$ .

# 3. RESULTS AND DISCUSSION

**3.1. Spatial Distribution of Street-Level Predictor Features.** The mean concentrations of BC and PN were 1.08  $\mu$ g/m³ and 6059 pt/cm³, respectively. The distribution of mobile monitoring data is shown in Figure S2. Figure S3 shows the spatial distribution of GSV images sampled around the mobile monitoring routes. Approximately 52 500 GSV images were collected for model development, including ~8800 GSV images collected within 50 m of the monitoring routes to capture central features and ~46 800 images within 2000 m to generate variables at various buffer radii. Corresponding to the

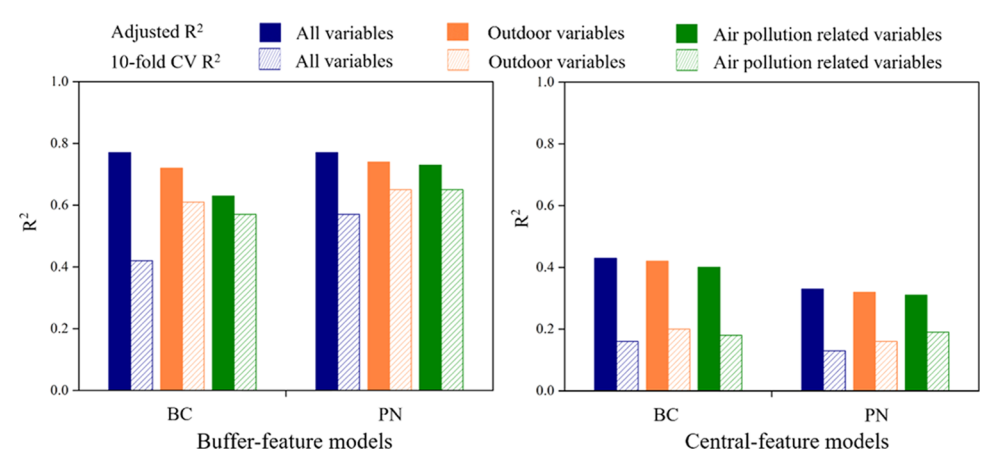


Figure 2. Comparison of model performance using theory-driven feature selection. Models developed with different categories of predictor variables are shown by color. Solid columns represent model adjusted  $R^2$ ; hashed columns represent 10-fold cross-validation  $R^2$ .

two sources of the GSV imagery, Google (i.e., collecting images while GSV cars driving along roads) and Google users' uploading photos, GSV images were mostly distributed along the road network or locations with more human activities. Since GSV images were predominantly on the road network, portions of the mobile monitoring routes (e.g., off-street trails far from major roads) did not have GSV images within 50 m (11.6% of the mobile monitoring aggregation locations). Thus, we excluded these monitoring locations from our model building in this study.

A core advantage of GSV images is that they capture streetlevel built and natural environment features. Among the 150 features segmented by scene parsing, the top 10 most frequent features in Blacksburg were as follows: sky (average percent in images: 28.1%), road (25.8%), tree (24.3%), grass (10.8%), earth (2.7%), building (1.9%), plant (1.4%), sidewalk (1.3%), car (0.8%), and house (0.7%). To illustrate the spatial granularity of GSV features, road and tree (as indicators of traffic and green space) are shown in Figure S3. The distribution of roads matched well with the road network in Blacksburg and had higher values along higher-order roads (e.g., highways). The tree variable followed intuition and had higher values where there were large tracts of tree canopy or abundance of street trees. Tree cover was prone to systematic bias due to the way GSV images are collected. For example, large areas of tree cover exist in the NW corner of the study area, but they were not captured because this area has few roads and thus few GSV images. This bias is not the case for traffic-related variables (e.g., roads, cars, sidewalks) that are only located on the transportation network. Detailed descriptive statistics of the extracted GSV features are listed in Table S2.

**3.2. Model Results.** 3.2.1. Theory-Driven Models. Overall, we found good model performance for the GSV-only empirical models. As shown in Tables S3 and S4, the adjusted  $R^2$  (10-fold CV  $R^2$ ) for the buffer-feature models using all variables was 0.77 (0.42) and 0.77 (0.57) for BC and PN, respectively. The decrease in  $R^2$  after 10-fold cross validation was large, which can be explained by several factors. Stochastic effects could be significant as GSV images were sampled with very high spatial resolution and thus possibly reveal more landscape heterogeneity. More importantly, the scene parsing algorithm generates 150 features, which is likely unnecessary as many of these features are irrelevant to air pollution. To reduce the amount of spurious variables, we conducted theory-driven

feature selection and evaluated the change in model performance (Figure 2). As the selection criteria for including variables became more stringent, we generally observed a slight decrease in adjusted  $R^2$ , but importantly, a larger increase in 10-fold CV  $R^2$  which reduced the gap between the two metrics. For example, the gap for the unconstrained BC (PN) models (i.e., using all variables) was 0.35 (0.20) as compared to 0.07 (0.07) when using "Theory-driven: Air pollution-related variables." This finding indicates that the most stringent theory-driven models reduced overfitting as well as improved model stability and variable interpretability while maintaining satisfying model fits. The adjusted  $R^2$  (10-fold CV  $R^2$ ) of the buffer-feature models with only air pollution-related variables were 0.63 (0.57) and 0.73 (0.65) for BC and PN, respectively. As expected, the model results show improved rationality in terms of the selected variables for the theory-driven feature selection as compared to the unconstrained models (Tables S3 and S4). We observed a slight increase in RMSE as theory-driven feature selection became stricter. For example, RMSE for the BC models using all variables, only outdoor variables, and only air pollution-related variables were 0.20, 0.22, and 0.26  $\mu$ g/m<sup>3</sup>, respectively. This trend could be explained by the reduced overfitting for theory-driven models, which is consistent with the finding that theory-driven models have lower adjusted  $R^2$ but higher 10-fold  $R^2$  compared to unconstrained models.

To investigate the correlation of street-level features within the immediate vicinity of the mobile monitoring routes to particulate concentrations, central-feature models were developed. As shown in Figure 2, the adjusted  $R^2$  (10-fold CV  $R^2$ ) was 0.43 (0.16) for BC and 0.33 (0.13) for PN when using all variables. Similar trends to the buffer-feature models among different variable categories were also found for the centralfeature models (Figure 2). However, the decrease in model fit before and after cross validation was more drastic for the central-feature models, possibly owing to the fact that only a limited number of images within 50 m of mobile monitoring were used for generating central features. A sensitivity analysis was further developed to explore the influence of radius size used for defining central features. Figure S4 shows the performance of central-feature models developed using the air pollution-related variables at various spatial scales (i.e., from 250 to 1000 m). Both adjusted  $R^2$  and 10-fold CV  $R^2$  increased when the central features were extracted from larger areas. For example, when setting the central range to 250 m, the centralfeature models explained  $\sim$ 50% of the variance. Adjusted  $R^2$ 

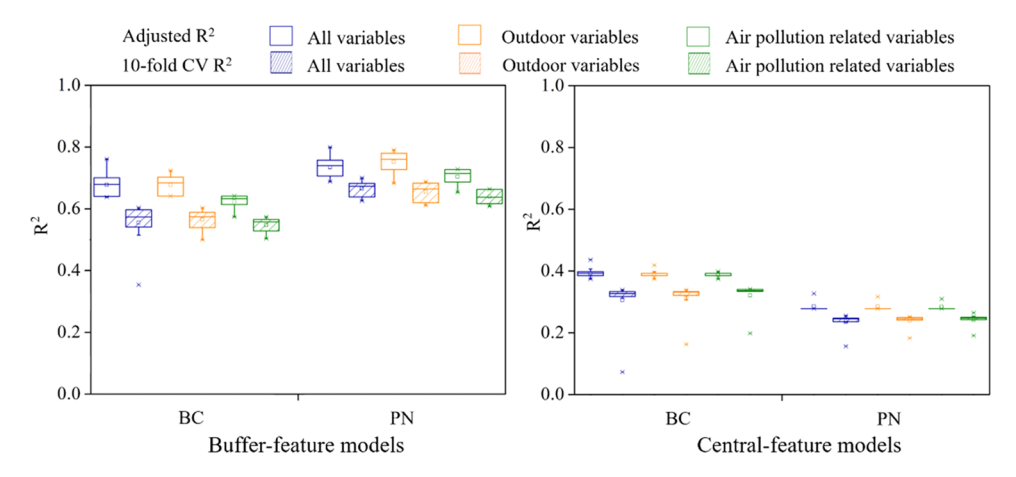


Figure 3. Model performance using integrated theory- and data-driven feature selection. Each box represents 15 scenarios for different categories of predictor variables. Models developed with different categories of predictor variables are shown by color. Hollow boxes represent model adjusted  $R^2$ ; hashed boxes represent 10-fold cross-validation  $R^2$ .

Table 1. Summary of Model Performance among All Model Types

	•						
pollutants	model type	feature selection method	predictor variables	number of selected variables	adjusted R <sup>2</sup>	10-fold CV R <sup>2</sup>	RMSE
BC $(\mu g/m^3)$	buffer-feature models	none	all variables	20	0.77	0.42	0.20
		theory-driven	outdoor variables	19	0.72	0.61	0.22
		theory-driven	air pollution-related variables	10	0.63	0.57	0.26
		data-driven	all variables	11-27	0.64 - 0.76	0.35 - 0.60	0.20 - 0.26
		integrated	outdoor variables	11-21	0.64 - 0.72	0.50 - 0.60	0.22 - 0.25
		integrated	air pollution-related variables	9-12	0.57-0.64	0.50 - 0.57	0.25 - 0.28
	central-feature models	none	all variables	9	0.43	0.16	0.32
		theory-driven	outdoor variables	10	0.42	0.20	0.32
		theory-driven	air pollution-related variables	8	0.40	0.18	0.33
		data-driven	all variables	5-13	0.37 - 0.44	0.07 - 0.34	0.32 - 0.34
		integrated	outdoor variables	5-10	0.37 - 0.42	0.16 - 0.34	0.32 - 0.34
		integrated	air pollution-related variables	5-8	0.37 - 0.40	0.20 - 0.34	0.33 - 0.34
	previous LUR models <sup>24</sup>	none	census data only; no GSV data	8	0.62	0.57	0.26 <sup>a</sup>
PN (pt/cm <sup>3</sup> )	buffer-feature models	none	all variables	15	0.77	0.57	821
		theory-driven	outdoor variables	12	0.74	0.65	916
		theory-driven	air pollution-related variables	17	0.73	0.65	954
		data-driven	all variables	7-22	0.69 - 0.80	0.63 - 0.70	807-1050
		integrated	outdoor variables	12-24	0.68 - 0.79	0.61-0.69	857-1005
		integrated	air pollution-related variables	11-17	0.65 - 0.73	0.61 - 0.66	941-1030
	central-feature models	none	all variables	12	0.33	0.13	1379
		theory-driven	outdoor variables	8	0.32	0.16	1391
		theory-driven	air pollution-related variables	7	0.31	0.19	1408
		data-driven	all variables	5-9	0.28-0.33	0.16-0.26	1379- 1461
		integrated	outdoor variables	5-8	0.28-0.32	0.18-0.25	1391- 1461
		integrated	air pollution-related variables	5-7	0.28-0.31	0.19-0.26	1408- 1461
	previous LUR models <sup>24</sup>	none	census data only; no GSV data	16	0.78	0.70	906 <sup>a</sup>

<sup>a</sup>RMSE for previous LUR models was calculated based on data from Hankey et al. <sup>24</sup>

(10-fold CV  $R^2$ ) increased to 0.51 (0.49) and 0.53 (0.48) for the BC model and the PN model. Prediction of PN concentrations was best using 250 m buffers and decreased at larger distances; the BC models showed little variability between 250 and 750 m. This finding suggests that these pollutants were strongly affected by the immediate surrounding environment at the magnitude of several hundred meters.

3.2.2. Data-Driven Models. Table S5 shows the number of predictor variables offered to our models using different feature selection methods. Although no prior knowledge of air pollution was applied, the number of predictor variables offered to the data-driven models among all scenarios (252–659 variables) aligned well with that of theory-driven models (279–513). Furthermore, we found a significant overlap of variables chosen by the two feature selection methods. For

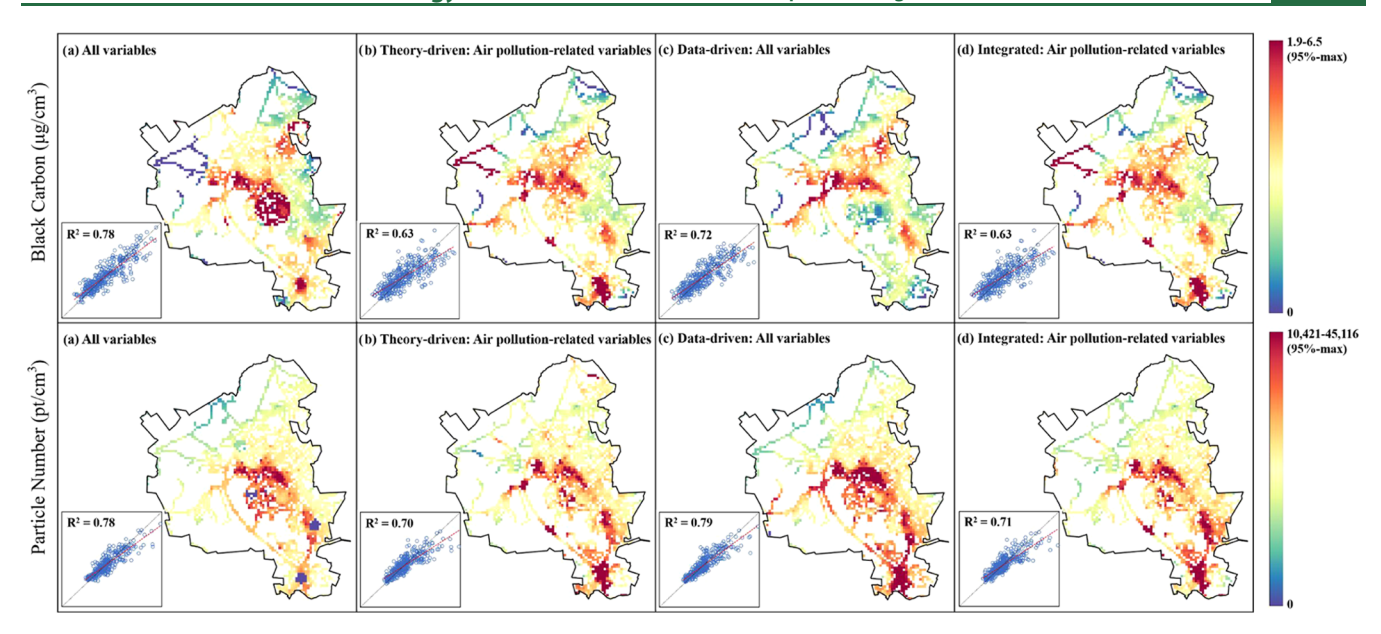


Figure 4. Estimated BC and PN concentrations using four types of GSV-only models. Only grid centroids with GSV images within 50 m are displayed. The scatterplots in the lower-left corner show model predicted air pollutant concentrations vs mobile monitoring air pollutant concentrations. The dashed red line is the best fit line; the dashed black line is the 1:1 line. Due to the highly right-skewed distributions of model estimates (Figure S7), we adjusted the color bar scale to visualize the spatial patterns of the models. Specifically, for each air pollutant, we binned the estimates among the four models and used the 95th percentile as the maximum for visualization.

example, 67-100% of "Theory driven: Air pollution-related variables" were also selected among the 15 data-driven scenarios. This demonstrates that even without background information on air quality, data-driven feature selection can achieve similar results to the theory-driven selection approach. Similar to the theory-driven models, the data-driven selection also showed the ability to enhance model robustness. Adjusted R<sup>2</sup> (10-fold CV R<sup>2</sup>) of buffer-feature models through datadriven selection was 0.64-0.76 (0.35-0.60) for BC and 0.69-0.80 (0.63-0.70) for PN (Figure S5). Compared to the unconstrained models, the data-driven models improved 10fold CV  $R^2$  significantly while maintaining high adjusted  $R^2$ . In addition, the 10-fold CV  $R^2$  was always the lowest in the least restrictive scenario, suggesting high multicollinearity when using too many variables. These trends were exacerbated in the central-feature models (Figure S6). For example, the 10-fold CV R<sup>2</sup> of the BC central-feature model of the least and most restrictive scenarios were 0.07 and 0.33, respectively. Assuming the best model had the highest 10-fold CV  $R^2$  among scenarios, adjusted R<sup>2</sup> (10-fold CV R<sup>2</sup>) of the best BC and PN bufferfeature models were 0.72 (0.60) and 0.80 (0.70), respectively. RMSE of the best BC and PN buffer-feature models were 0.22  $\mu g/m^3$  and 807 pt/cm<sup>3</sup>, respectively. Full model parameters are listed in Table S6. Although the model fits were improved by data-driven variable selection, a few irrelevant variables were still selected in the models, leading to reduced model interpretability.

3.2.3. Integrated Feature Selection Models. As expected, similar trends of improved model robustness and interpretability when using the theory- and data-driven feature selection methods were also observed using the integrated method (Figure 3). The best integrated models always outperformed or matched the corresponding theory-driven models showing the utility of using both theory- and data-driven feature selection. We also found that the buffer-feature models generally had better model fits for PN while the central-feature models showed better performance for BC. This finding suggests that

the effect of the street-level environment on BC was greater than on PN. This is reasonable since the dominant sources of BC are primary emissions related to combustion processes, <sup>42</sup> while particles can be either emitted directly or generated from secondary sources (e.g., precursors of photochemical reactions <sup>43,44</sup>).

3.3. Comparison among Models. Table 1 shows model performance for all GSV-only models as well as the previously published LUR models.<sup>24</sup> In general, GSV-only models had a comparable model performance to LUR models using traditional GIS-derived variables. For buffer-feature models with only air pollution-related variables (best for interpretability), the 10-fold CV R<sup>2</sup> after integrated feature selection was as high as 0.57 for BC and 0.66 for PN. If pursuing the best goodness-of-fit and neglecting the theoretical basis of predictor variables, we can achieve better model fits. For example, the best data-driven models showed higher adjusted  $R^2$  (10-fold CV  $R^2$ ) and lower RMSE as compared to previous LUR models using traditional predictors. Our models suggest that features extracted from GSV images can be used to successfully develop predictive models in a variety of ways depending on the user's purpose, e.g., either pursuing best goodness-of-fit regardless of model interpretability or to be consistent with theory as much as possible.

We chose a subset of buffer-feature models to estimate BC and PN concentrations for the entire study area (~63 000 GSV images): (1) models based on all variables, (2) theory-driven models based on air pollution-related variables, (3) the best data-driven models, and (4) the best integrated theory- and data-driven models based on air pollution-related variables. Concentrations were mapped on a 100 m × 100 m grid in Figure 4. Due to the limitation of GSV images mainly being captured along roadways, we were only able to make predictions for 39% of Blacksburg's land area. Figure 4 also includes scatterplots of predicted vs observed concentrations. In general, all models showed good agreement between model predictions and mobile monitoring data. The overall spatial

patterns of estimated concentrations were similar among models, especially for areas where GSV images were more densely distributed. A few inconsistencies were apparent, for example, the SE corner of Blacksburg was estimated to have extremely low concentrations by the unconstrained PN model but was a hotspot using other models. Based on a review of these models, we found that the low estimates resulted from some portions of GSV images being misclassified into the class "bed"—a feature that is highly unlikely to appear frequently in outdoor images. Given that this area is an intersection of several major roads, it is expected to have elevated concentrations in this area. This example illustrates the importance of using feature selection to remove spurious predictor variables prior to building empirical models. Similar problems appeared in the NW corner of the map. In this case, the inconsistent predictions for BC concentrations mainly resulted from the sparsity of GSV images in that region along with a few unusual GSV features. Considering both the theoretical basis of input variables and model accuracy, we suggest using models with integrated variable selection for broader model applications.

Although the application of our models was limited by the availability of GSV images, alternative models could be constructed to mitigate this problem. For example, we developed reduced buffer-feature models using only larger buffer radii (full details are described in the SI), and the models maintained good model performance (Table S7). For example, adjusted  $R^2$  (10-fold CV  $R^2$ ) of the best models with radii 500 m or greater were 0.60 (0.53) for BC and 0.62 (0.56) for PN. Since 81% of the grid centroids for prediction had GSV images within 250 m (94% when the radius was 500 m), we applied the reduced buffer-feature models to a wider land area of Blacksburg to generate air pollution estimates (Figure S8). These models showed reasonably consistent spatial patterns to the LUR models from our previous work.<sup>24</sup> In general, the hotspots identified by the LUR models with traditional GISderived variables were mainly distributed along major roads. While GSV-only models also revealed these hotspots, our proposed models further identified other localized regions with high BC or PN concentrations that the GIS-derived models did not. For example, at the intersection of several major roads in the SE corner of Blacksburg, both GSV-only models and the previous LUR models estimated elevated PN concentrations in this region, while only the GSV-only models identified it as a BC hotspot as well. Future work may collect field observations in these potential hotspots to evaluate our new modeling approach.

**3.4.** Results of Spatial Autocorrelation Analysis and Model Uncertainty. To compare among our models, we assessed spatial autocorrelation of model residuals and model uncertainty (full details are described in the SI). Briefly, our model residuals demonstrate at least some spatial autocorrelation, partly due to the fine spatial resolution of the mobile monitoring data and GSV images (Table S8 and Figure S9). Compared with the previous LUR models using traditional predictors, GSV-only models show slightly higher standard error (Figures S10 and S11). A useful direction for future research is to use more advanced modeling approaches to account for spatial autocorrelation issues and reduce model uncertainty.

#### 4. LIMITATIONS AND IMPLICATIONS

The usefulness of GSV-only models depends on the availability and quality of GSV images for any given region. In less developed or rural regions, this approach may miss large tracts of land where there is no road access and thus no GSV imagery. In addition, GSV images are static and in many areas are not updated at the same rate as urban development. Although we prioritized sampling GSV images from the same year of air quality monitoring, only 12% of GSV images retrieved were photographed in 2016. The impact of this temporal mismatch could be large or small depending on the rate of change of the built environment. Future work could apply our approach in urban areas where larger amounts of GSV images are available and updated more frequently. Given the continually growing repositories of public streetscape imagery,<sup>33</sup> this limitation is expected to be mitigated in the future.

Introducing better temporal resolution is another important goal for accurate exposure assessment. 24,45,46 While finer spatial resolution can be achieved using GSV imagery, improving temporal resolution is a challenge in the short run. Multiple studies have used satellite imagery to map air pollution with high spatial-temporal resolution. 47-49 A possible solution is to use both GSV images and satellite imagery for model development. By combining remote sensing imagery (which can achieve daily updates) and ground-level imagery, both model accuracy and spatiotemporal precision may be leveraged as multiview aspects of the built environment could be used. 50,51 Another limitation is that the performance of the image processing technique (in this case PSPNet) for feature extraction also determines the performance of the image-based air quality models. Our results show that feature selection can successfully reduce the number of spurious variables, which reduced issues caused by overcomplicated semantic segmentation or misclassification. Given the rapid development in computer vision and deep learning, 52,53 future work may also explore improved algorithms to reduce misclassification during scene parsing.

Our study suggests that GSV imagery alone, and thus likely any other large street scene imagery data set with high resolution and broad coverage, may provide sufficient information to characterize air pollution patterns. Imagery based data sources offer potentially three major advantages: (1) finer spatial (i.e., street-level) resolution, (2) the ability to apply consistent data collection and processing protocols across large geographies and political boundaries, and (3) flexibility in method of data reduction for model development and application. The development of low-cost and portable sensors in conjunction with increased efforts to explore mobile monitoring provides an opportunity to characterize the spatial variability of air pollution at the street level. 54,55 Our proposed modeling approach leverages the strengths of mobile monitoring and GSV images in characterizing street-level gradients of air pollution. Our model results also highlight the impact of street-level factors (e.g., built environment, local emission sources) on air quality, which suggests highly localized interventions may yield reductions in exposure. As low-cost air quality sensors and street scene images become more ubiquitous, the combination of mobile monitoring and automated street-level image analysis could become a scalable framework that could be applied nearly anywhere in the world

as a tool to track air pollution exposure and disparities at small spatial scales.

## ASSOCIATED CONTENT

# Supporting Information

The Supporting Information is available free of charge at https://pubs.acs.org/doi/10.1021/acs.est.0c05572.

Information on the description of data-driven feature selection; reduced GSV-only models; and results of spatial autocorrelation analysis and model uncertainty (Tables S1–S8 and Figures S1–S11) (PDF)

#### AUTHOR INFORMATION

#### Corresponding Author

Steve Hankey — School of Public and International Affairs, Virginia Tech, Blacksburg, Virginia 24061, United States; occid.org/0000-0002-7530-6077; Email: hankey@vt.edu

#### **Author**

Meng Qi — School of Public and International Affairs, Virginia Tech, Blacksburg, Virginia 24061, United States;
orcid.org/0000-0003-0700-2773

Complete contact information is available at: https://pubs.acs.org/10.1021/acs.est.0c05572

#### Notes

The authors declare no competing financial interest.

#### ACKNOWLEDGMENTS

This material is based upon work supported by the National Science Foundation under Grant no. CBET 1943705. The Virginia Tech BioBuild Interdisciplinary Graduate Education Program also supported this work.

## REFERENCES

- (1) Pope, C. A.; Ezzati, M.; Dockery, D. W. Fine-Particulate Air Pollution and Life Expectancy in the United States. *N. Engl. J. Med.* **2009**, *360*, *376*–*386*.
- (2) Hoek, G.; Krishnan, R. M.; Beelen, R.; Peters, A.; Ostro, B.; Brunekreef, B.; Kaufman, J. D. Long-term air pollution exposure and cardio- respiratory mortality: a review. *Environ. Health* **2013**, *12*, 43.
- (3) Kim, K. H.; Kabir, E.; Kabir, S. A review on the human health impact of airborne particulate matter. *Environ. Int.* **2015**, *74*, 136–143.
- (4) Shi, L. H.; Zanobetti, A.; Kloog, I.; Coull, B. A.; Koutrakis, P.; Melly, S. J.; Schwartz, J. D. Low-Concentration PM<sub>2.5</sub> and Mortality: Estimating Acute and Chronic Effects in a Population-Based Study. *Environ. Health Perspect.* **2016**, *124*, 46–52.
- (5) Apte, J. S.; Messier, K. P.; Gani, S.; Brauer, M.; Kirchstetter, T. W.; Lunden, M. M.; Marshall, J. D.; Portier, C. J.; Vermeulen, R. C. H.; Hamburg, S. P. High-Resolution Air Pollution Mapping with Google Street View Cars: Exploiting Big Data. *Environ. Sci. Technol.* 2017, *51*, 6999–7008.
- (6) Miller, D. J.; Actkinson, B.; Padilla, L.; Griffin, R. J.; Moore, K.; Lewis, P. G. T.; Gardner-Frolick, R.; Craft, E.; Portier, C. J.; Hamburg, S. P.; Alvarez, R. A. Characterizing Elevated Urban Air Pollutant Spatial Patterns with Mobile Monitoring in Houston, Texas. *Environ. Sci. Technol.* **2020**, *54*, 2133–2142.
- (7) Alexeeff, S. E.; Roy, A.; Shan, J.; Liu, X.; Messier, K.; Apte, J. S.; Portier, C.; Sidney, S.; Van Den Eeden, S. K. High-resolution mapping of traffic related air pollution with Google street view cars and incidence of cardiovascular events within neighborhoods in Oakland, CA. *Environ. Health* **2018**, *17*, 38.
- (8) Lee, H. J. Benefits of High Resolution PM<sub>2.5</sub> Prediction using Satellite MAIAC AOD and Land Use Regression for Exposure

- Assessment: California Examples. Environ. Sci. Technol. 2019, 53, 12774–12783.
- (9) Faridi, S.; Shamsipour, M.; Krzyzanowski, M.; Kunzli, N.; Amini, H.; Azimi, F.; Malkawi, M.; Momeniha, F.; Gholampour, A.; Hassanvand, M. S.; Naddafi, K. Long-term trends and health impact of PM<sub>2.5</sub> and O<sub>3</sub> in Tehran, Iran, 2006-2015. *Environ. Int.* **2018**, *114*, 37–49.
- (10) Vineis, P.; Hoek, G.; Krzyzanowski, M.; Vigna-Taglianti, F.; Veglia, F.; Airoldi, L.; Autrup, H.; Dunning, A.; Garte, S.; Hainaut, P.; Malaveille, C.; Matullo, G.; Overvad, K.; Raaschou-Nielsen, O.; Clavel-Chapelon, F.; Linseisen, J.; Boeing, H.; Trichopoulou, A.; Palli, D.; Peluso, M.; Krogh, V.; Tumino, R.; Panico, S.; Bueno-De-Mesquita, H. B.; Peeters, P. H.; Lund, E. E.; Gonzalez, C. A.; Martinez, C.; Dorronsoro, M.; Barricarte, A.; Cirera, L.; Quiros, J. R.; Berglund, G.; Forsberg, B.; Day, N. E.; Key, T. J.; Saracci, R.; Kaaks, R.; Riboli, E. Air pollution and risk of lung cancer in a prospective study in Europe. *Int. J. Cancer* 2006, 119, 169–174.
- (11) Ma, Z. W.; Hu, X. F.; Sayer, A. M.; Levy, R.; Zhang, Q.; Xue, Y. G.; Tong, S. L.; Bi, J.; Huang, L.; Liu, Y. Satellite-Based Spatiotemporal Trends in PM<sub>2.5</sub> Concentrations: China, 2004-2013. *Environ. Health Perspect.* **2016**, *124*, 184–192.
- (12) Sickles, J. E.; Shadwick, D. S. Air quality and atmospheric deposition in the eastern US: 20 years of change. *Atmos. Chem. Phys.* **2015**, *15*, 173–197.
- (13) Larson, T.; Henderson, S. B.; Brauer, M. Mobile Monitoring of Particle Light Absorption Coefficient in an Urban Area as a Basis for Land Use Regression. *Environ. Sci. Technol.* **2009**, *43*, 4672–4678.
- (14) Solomon, P. A.; Crumpler, D.; Flanagan, J. B.; Jayanty, R. K. M.; Rickman, E. E.; McDade, C. E. US National PM<sub>2.5</sub> Chemical Speciation Monitoring Networks-CSN and IMPROVE: Description of networks. *J. Air Waste Manage. Assoc.* **2014**, *64*, 1410–1438.
- (15) Kumar, P.; Morawska, L.; Martani, C.; Biskos, G.; Neophytou, M.; Di Sabatino, S.; Bell, M.; Norford, L.; Britter, R. The rise of low-cost sensing for managing air pollution in cities. *Environ. Int.* **2015**, *75*, 199–205.
- (16) Minet, L.; Liu, R.; Valois, M. F.; Xu, J. S.; Weichenthal, S.; Hatzopoulou, M. Development and Comparison of Air Pollution Exposure Surfaces Derived from On-Road Mobile Monitoring and Short-Term Stationary Sidewalk Measurements. *Environ. Sci. Technol.* **2018**, *52*, 3512–3519.
- (17) Eeftens, M.; Beelen, R.; de Hoogh, K.; Bellander, T.; Cesaroni, G.; Cirach, M.; Declercq, C.; Dedele, A.; Dons, E.; de Nazelle, A.; Dimakopoulou, K.; Eriksen, K.; Falq, G.; Fischer, P.; Galassi, C.; Grazuleviciene, R.; Heinrich, J.; Hoffmann, B.; Jerrett, M.; Keidel, D.; Korek, M.; Lanki, T.; Lindley, S.; Madsen, C.; Molter, A.; Nador, G.; Nieuwenhuijsen, M.; Nonnemacher, M.; Pedeli, X.; Raaschou-Nielsen, O.; Patelarou, E.; Quass, U.; Ranzi, A.; Schindler, C.; Stempfelet, M.; Stephanou, E.; Sugiri, D.; Tsai, M. Y.; Yli-Tuomi, T.; Varro, M. J.; Vienneau, D.; von Klot, S.; Wolf, K.; Brunekreef, B.; Hoek, G. Development of Land Use Regression Models for PM<sub>2.5</sub>, PM<sub>2.5</sub> Absorbance, PM<sub>10</sub> and PM<sub>coarse</sub> in 20 European Study Areas; Results of the ESCAPE Project. *Environ. Sci. Technol.* **2012**, *46*, 11195–11205.
- (18) Schmitz, O.; Beelen, R.; Strak, M.; Hoek, G.; Soenario, I.; Brunekreef, B.; Vaartjes, I.; Dijst, M. J.; Grobbee, D. E.; Karssenberg, D. Data Descriptor: High resolution annual average air pollution concentration maps for the Netherlands. *Sci. Data* **2019**, *6*, No. 190035.
- (19) Larkin, A.; Geddes, J. A.; Martin, R. V.; Xiao, Q. Y.; Liu, Y.; Marshall, J. D.; Brauer, M.; Hystad, P. Global Land Use Regression Model for Nitrogen Dioxide Air Pollution. *Environ. Sci. Technol.* **2017**, *51*, *6957–6964*.
- (20) Shi, Y.; Lau, K. K. L.; Ng, E. Developing Street-Level  $PM_{2.5}$  and  $PM_{10}$  Land Use Regression Models in High-Density Hong Kong with Urban Morphological Factors. *Environ. Sci. Technol.* **2016**, *50*, 8178–8187
- (21) Hoek, G.; Beelen, R.; de Hoogh, K.; Vienneau, D.; Gulliver, J.; Fischer, P.; Briggs, D. A review of land-use regression models to assess

- spatial variation of outdoor air pollution. *Atmos. Environ.* **2008**, *42*, 7561–7578.
- (22) Hankey, S.; Marshall, J. D. Land Use Regression Models of On-Road Particulate Air Pollution (Particle Number, Black Carbon, PM<sub>2.5</sub>, Particle Size) Using Mobile Monitoring. *Environ. Sci. Technol.* **2015**, *49*, 9194–9202.
- (23) Messier, K. P.; Chambliss, S. E.; Gani, S.; Alvarez, R.; Brauer, M.; Choi, J. J.; Hamburg, S. P.; Kerckhoffs, J.; LaFranchi, B.; Lunden, M. M.; Marshall, J. D.; Portier, C. J.; Roy, A.; Szpiro, A. A.; Vermeulen, R. C. H.; Apte, J. S. Mapping Air Pollution with Google Street View Cars: Efficient Approaches with Mobile Monitoring and Land Use Regression. *Environ. Sci. Technol.* **2018**, *52*, 12563–12572.
- (24) Hankey, S.; Sforza, P.; Pierson, M. Using Mobile Monitoring to Develop Hourly Empirical Models of Particulate Air Pollution in a Rural Appalachian Community. *Environ. Sci. Technol.* **2019**, 53, 4305–4315.
- (25) Hatzopoulou, M.; Valois, M. F.; Levy, I.; Mihele, C.; Lu, G.; Bagg, S.; Minet, L.; Brook, J. Robustness of Land-Use Regression Models Developed from Mobile Air Pollutant Measurements. *Environ. Sci. Technol.* **2017**, *51*, 3938–3947.
- (26) Rundle, A. G.; Bader, M. D. M.; Richards, C. A.; Neckerman, K. M.; Teitler, J. O. Using Google Street View to Audit Neighborhood Environments. *Am. J. Prev. Med.* **2011**, *40*, 94–100.
- (27) Hong, K. Y.; Pinheiro, P. O.; Minet, L.; Hatzopoulou, M.; Weichenthal, S. Extending the spatial scale of land use regression models for ambient ultrafine particles using satellite images and deep convolutional neural networks. *Environ. Res.* **2019**, *176*, No. 108513.
- (28) Rzotkiewicz, A.; Pearson, A. L.; Dougherty, B. V.; Shortridge, A.; Wilson, N. Systematic review of the use of Google Street View in health research: Major themes, strengths, weaknesses and possibilities for future research. *Health Place* **2018**, *52*, 240–246.
- (29) Charreire, H.; Mackenbach, J. D.; Ouasti, M.; Lakerveld, J.; Compernolle, S.; Ben-Rebah, M.; McKee, M.; Brug, J.; Rutter, H.; Oppert, J. M. Using remote sensing to define environmental characteristics related to physical activity and dietary behaviours: A systematic review (the SPOTLIGHT project). *Health Place* **2014**, 25, 1–9.
- (30) Gebru, T.; Krause, J.; Wang, Y. L.; Chen, D. Y.; Deng, J.; Aiden, E. L.; Li, F. F. Using deep learning and Google Street View to estimate the demographic makeup of neighborhoods across the United States. *Proc. Natl. Acad. Sci. U.S.A.* **2017**, *114*, 13108–13113.
- (31) Gong, F. Y.; Zeng, Z. C.; Zhang, F.; Li, X. J.; Ng, E.; Norford, L. K. Mapping sky, tree, and building view factors of street canyons in a high-density urban environment. *Build. Environ.* **2018**, *134*, 155–167.
- (32) Zhao, H. S.; Shi, J. P.; Qi, X. J.; Wang, X. G.; Jia, J. Y. Pyramid Scene Parsing Network. *Proc. IEEE Conf. Comput. Vis. Pattern Recognit.* 2017, 6230–6239.
- (33) Li, X. J.; Zhang, C. R.; Li, W. D.; Ricard, R.; Meng, Q. Y.; Zhang, W. X. Assessing street-level urban greenery using Google Street View and a modified green view index. *Urban For. Urban Green.* **2015**, *14*, 675–685.
- (34) Stubbings, P.; Peskett, J.; Rowe, F.; Arribas-Bel, D. A Hierarchical Urban Forest Index Using Street-Level Imagery and Deep Learning. *Remote Sens.* **2019**, *11*, 1395.
- (35) Seiferling, I.; Naik, N.; Ratti, C.; Proulx, R. Green streets Quantifying and mapping urban trees with street-level imagery and computer vision. *Landscape Urban Plann.* **2017**, *165*, 93–101.
- (36) Bader, M. D. M.; Mooney, S. J.; Lee, Y. J.; Sheehan, D.; Neckerman, K. M.; Rundle, A. G.; Teitler, J. O. Development and deployment of the Computer Assisted Neighborhood Visual Assessment System (CANVAS) to measure health-related neighborhood conditions. *Health Place* **2015**, *31*, 163–172.
- (37) Li, X. J.; Zhang, C. R.; Li, W. D. Building block level urban land-use information retrieval based on Google Street View images. *GISci. Remote Sens.* **2017**, *54*, 819–835.
- (38) Naik, N.; Kominers, S. D.; Raskar, R.; Glaeser, E. L.; Hidalgo, C. A. Computer vision uncovers predictors of physical urban change. *Proc. Natl. Acad. Sci. U.S.A.* **2017**, *114*, 7571–7576.

- (39) Ganji, A.; Minet, L.; Weichenthal, S.; Hatzopoulou, M. Predicting traffic-related air pollution using feature extraction from built environment images. *Environ. Sci. Technol.* **2020**, 10688–10699.
- (40) Raghu, V. K.; Ge, X. Y.; Chrysanthis, P. K.; Benos, P. V. In *Integrated Theory- and Data-driven Feature Selection in Gene Expression Data Analysis*, 2017 IEEE 33rd International Conference on Data Engineering; IEEE, 2017; pp 1525–1532.
- (41) Karpatne, A.; Atluri, G.; Faghmous, J. H.; Steinbach, M.; Banerjee, A.; Ganguly, A.; Shekhar, S.; Samatova, N.; Kumar, V. Theory-Guided Data Science: A New Paradigm for Scientific Discovery from Data. *IEEE Trans. Knowl. Data Eng.* **2017**, 29, 2318–2331.
- (42) Bond, T. C.; Doherty, S. J.; Fahey, D. W.; Forster, P. M.; Berntsen, T.; DeAngelo, B. J.; Flanner, M. G.; Ghan, S.; Karcher, B.; Koch, D.; Kinne, S.; Kondo, Y.; Quinn, P. K.; Sarofim, M. C.; Schultz, M. G.; Schulz, M.; Venkataraman, C.; Zhang, H.; Zhang, S.; Bellouin, N.; Guttikunda, S. K.; Hopke, P. K.; Jacobson, M. Z.; Kaiser, J. W.; Klimont, Z.; Lohmann, U.; Schwarz, J. P.; Shindell, D.; Storelvmo, T.; Warren, S. G.; Zender, C. S. Bounding the role of black carbon in the climate system: A scientific assessment. *J. Geophys. Res.: Atmos.* 2013, 118, 5380–5552.
- (43) Klimont, Z.; Kupiainen, K.; Heyes, C.; Purohit, P.; Cofala, J.; Rafaj, P.; Borken-Kleefeld, J.; Schopp, W. Global anthropogenic emissions of particulate matter including black carbon. *Atmos. Chem. Phys.* **2017**, *17*, 8681–8723.
- (44) Hu, W.; Hu, M.; Hu, W. W.; Zheng, J.; Chen, C.; Wu, Y. S.; Guo, S. Seasonal variations in high time-resolved chemical compositions, sources, and evolution of atmospheric submicron aerosols in the megacity Beijing. *Atmos. Chem. Phys.* **2017**, *17*, 9979–10000
- (45) Nyhan, M.; Grauwin, S.; Britter, R.; Misstear, B.; McNabola, A.; Laden, F.; Barrett, S. R. H.; Ratti, C. "Exposure Track" The Impact of Mobile-Device-Based Mobility Patterns on Quantifying Population Exposure to Air Pollution. *Environ. Sci. Technol.* **2016**, *50*, 9671–9681.
- (46) Stafoggia, M.; Schwartz, J.; Badaloni, C.; Bellander, T.; Alessandrini, E.; Cattani, G.; de' Donato, F.; Gaeta, A.; Leone, G.; Lyapustin, A.; Sorek-Hamer, M.; de Hoogh, K.; Di, Q.; Forastiere, F.; Kloog, I. Estimation of daily PM<sub>10</sub> concentrations in Italy (2006-2012) using finely resolved satellite data, land use variables and meteorology. *Environ. Int.* 2017, 99, 234–244.
- (47) He, Q. Q.; Huang, B. Satellite-based mapping of daily high-resolution ground  $PM_{2.5}$  in China via space-time regression modeling. *Remote Sens. Environ.* **2018**, 206, 72–83.
- (48) Di, Q.; Kloog, I.; Koutrakis, P.; Lyapustin, A.; Wang, Y. J.; Schwartz, J. Assessing  $PM_{2.5}$  Exposures with High Spatiotemporal Resolution across the Continental United States. *Environ. Sci. Technol.* **2016**, *50*, 4712–4721.
- (49) Lv, B. L.; Hu, Y. T.; Chang, H. H.; Russell, A. G.; Bai, Y. Q. Improving the Accuracy of Daily  $PM_{2.5}$  Distributions Derived from the Fusion of Ground-Level Measurements with Aerosol Optical Depth Observations, a Case Study in North China. *Environ. Sci. Technol.* **2016**, *50*, 4752–4759.
- (50) Lefevre, S.; Tuia, D.; Wegner, J. D.; Produit, T.; Nassar, A. S. Toward Seamless Multiview Scene Analysis From Satellite to Street Level. *Proc. IEEE* **2017**, *105*, 1884–1899.
- (51) Weichenthal, S.; Hatzopoulou, M.; Brauer, M. A picture tells a thousand...exposures: Opportunities and challenges of deep learning image analyses in exposure science and environmental epidemiology. *Environ. Int.* **2019**, *122*, 3–10.
- (52) Guo, Y. M.; Liu, Y.; Oerlemans, A.; Lao, S. Y.; Wu, S.; Lew, M. S. Deep learning for visual understanding: A review. *Neurocomputing* **2016**, *187*, 27–48.
- (53) Ma, L.; Liu, Y.; Zhang, X. L.; Ye, Y. X.; Yin, G. F.; Johnson, B. A. Deep learning in remote sensing applications: A meta-analysis and review. ISPRS J. Photogramm. Remote Sens. 2019, 152, 166–177.
- (54) Lim, C. C.; Kim, H.; Vilcassim, M. J. R.; Thurston, G. D.; Gordon, T.; Chen, L. C.; Lee, K.; Heimbinder, M.; Kim, S. Y. Mapping urban air quality using mobile sampling with low-cost

sensors and machine learning in Seoul, South Korea. *Environ. Int.* **2019**, *131*, No. 105022.

(55) Morawska, L.; Thai, P. K.; Liu, X. T.; Asumadu-Sakyi, A.; Ayoko, G.; Bartonova, A.; Bedini, A.; Chai, F. H.; Christensen, B.; Dunbabin, M.; Gao, J.; Hagler, G. S. W.; Jayaratne, R.; Kumar, P.; Lau, A. K. H.; Louie, P. K. K.; Mazaheri, M.; Ning, Z.; Motta, N.; Mullins, B.; Rahman, M. M.; Ristovski, Z.; Shafiei, M.; Tjondronegoro, D.; Westerdahl, D.; Williams, R. Applications of low-cost sensing technologies for air quality monitoring and exposure assessment: How far have they gone? *Environ. Int.* 2018, 116, 286—299.